Solar disk gamma-ray emission via synthetic magnetic turbulence canopy from photosphere to low corona

Eleonora Puzzoni,[a,b] **Federico Fraschetti,**[a,c,*] **József Kóta**[a] **and Joe Giacalone**[a]

[a]*University of Arizona, Lunar and Planetary Laboratory,*
1629 E University Blvd, Tucson, AZ, USA

[b]*Observatoire de la Côte d'Azur, Laboratoire Lagrange,*
Bd de l'Observatoire, CS 34229, 06304 Nice cedex 4, France3

[c]*Center for Astrophysics, Harvard & Smithsonian,*
60 Garden Street, Cambridge, MA, USA
E-mail: epuzzoni@arizona.edu, federico.fraschetti@cfa.harvard.edu,
jkota@arizona.edu, giacalon@arizona.edu

Gamma-ray emission in the GeV-TeV range from the solar disk (observed by Fermi-LAT and HAWC) is likely to arise from collisions of galactic cosmic rays (GCRs) with solar atmospheric plasma. We model the photo-/chromospheric magnetic field with a static, laminar structure of open field lines in the chromosphere increasingly braiding near the solar surface, with a typical scale height of 0.01 solar radii. The height-dependent increase in magnetic turbulence strength is modulated by an exponential scalar function. Employing 3D test-particle numerical simulations (with PLUTO code) and empirical models for hadronic inelastic collisions, we investigate how such distorted magnetic field lines affect the gamma-rays flux by injecting GeV-TeV protons into both laminar and turbulent regions, as a function of the turbulence strength. Our findings show that the turbulent magnetic structures can account for the gamma-ray spectrum observed by Fermi-LAT/HAWC, in producing a nearly power law dependence on energy. A rebrightening between approximately 30 and 100 GeV (following a yet unexplained ~ 30 GeV spectral dip), suggests an enhanced confinement within the photo-/chromospheric layer.

---

*Speaker

1. Introduction

Recent years have seen growing interest in high-energy gamma-ray emission from the solar disk, following the pioneering theoretical work of [1] (hereafter SSG91). Their model attributed the emission to galactic cosmic rays (GCRs) mirroring in solar magnetic fields and interacting with the solar atmosphere. However, observations from Fermi-LAT (covering 20 MeV to 300 GeV) and HAWC (sensitive from 100 GeV to 10 TeV) revealed significantly stronger and higher-energy gamma-ray emission than originally predicted. In particular, the observed flux near 1 GeV exceeded theoretical expectations by a factor of ~ 7 [2], with Fermi-LAT detecting photons up to several hundred GeV [3], and HAWC further extending the observed energy range into the TeV domain [4]. Notably, the emission shows a strong anticorrelation with solar activity [5–7] and energy-dependent anisotropies [6, 8]. Moreover, an unexpected dip at ~ 30 GeV has been observed [6, 9], while it remains absent in the CALorimetric Electron Telescope (CALET) data [10].

These findings have motivated several revisions and extensions to the SSG91 framework, emphasizing the role of magnetic field structures in the photo- and chromo-sphere [11–15]. In particular, [13] was the first to investigate the role of closed magnetic structures (specifically, magnetic arcades) in trapping GCRs and contributing to gamma-ray emission. However, the connection between the open magnetic field lines, which guide particles into the solar atmosphere, and these closed structures remained unresolved.

Building on [13], we investigate the impact of small-scale magnetic distortions in the photo- and chromo-sphere through a synthetic 3D magnetic field model. This setup captures the gradual transition from radial open-field configurations to braided, near-closed structures, in line with expected behavior from granular flows and/or MHD turbulence [see, e.g., 16]. While not dynamically generated, the model reproduces field structures and strengths (from 100 G up to 1 kG) consistent with both MHD simulations and solar remote-sensing observations [17–20]. We use this framework to simulate the propagation of GCR protons as test-particles with the PLUTO code [21], with the goal of examining how their trajectories are shaped by the transition from open to increasingly complex, braided magnetic field structures near the solar surface, and how this affects their contribution to the observed gamma-ray flux.
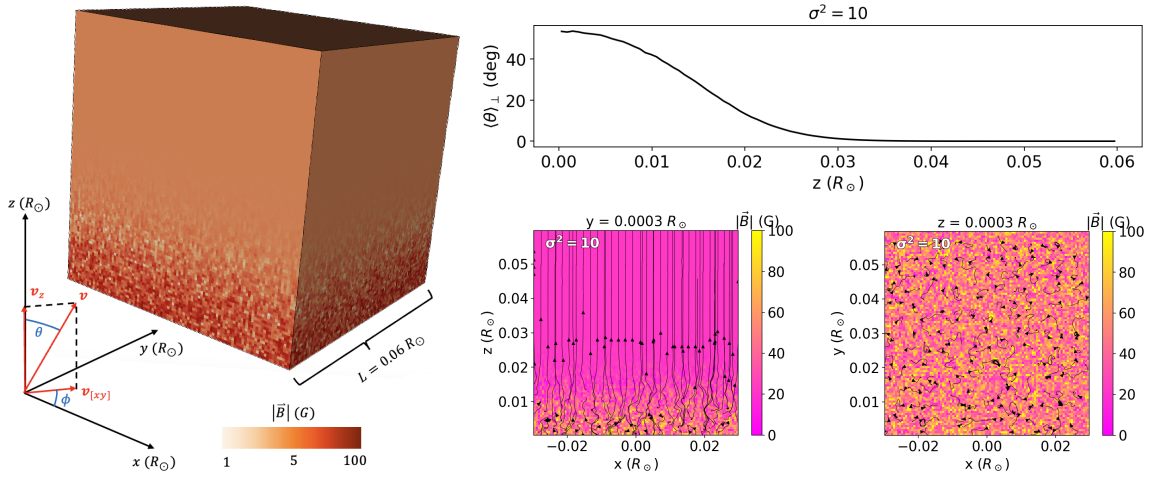
2. Magnetic field model

The total magnetic field is given by

$$\mathbf{B}(x, y, z) = B_0\hat{\mathbf{k}} + f(z)\nabla \times \mathbf{S}(x, y, z) + \nabla f(z) \times \mathbf{S}(x, y, z), \tag{1}$$

where $B_0 = 5 - 50$ G is the chromosphere/low corona constant magnetic field along the z-direction [consistent with both MHD simulations and Daniel K. Inouye Solar Telescope, DKIST, spectropolarimetric measurements 22, 23], leading to a maximum photospheric magnetic field strength of $B_{\max} \sim 100 - 1000$ G respectively [in agreement with remote sensing observations 17, 18], $f(z)e^{-(z/\Lambda)^2}$ (with scale height $\Lambda \simeq 1.41 \times 10^{-2} R_\odot$) is an arbitrary scalar function modulating the onset of the magnetic braiding along z, while $\mathbf{S}(x, y, z)$ is the vector potential derived in [24] associated with the synthetic magnetic field $\delta\mathbf{B}(x, y, z)$ from [25], i.e., $\delta\mathbf{B}(x, y, z) = \nabla \times \mathbf{S}(x, y, z)$. The total 3D magnetic field structure is shown in the left plot of Fig. 1, illustrating that the field

remains predominantly vertical in the low corona and chromosphere and becomes increasingly braided only as it approaches the photosphere. The deviation from the vertical field is quantified by the average angle $\langle\theta\rangle_\perp = \arctan(\sqrt{B_x^2(x,y,z) + B_y^2(x,y,z)}/B_0)$, which is shown in the upper right panel of Fig. 1 as a function of altitude z [also shown by 17, 18]. The lower right panels of Fig. 1 show the magnetic field magnitude and field lines in the lowest xy-plane (right, corresponding to the bottom of the photosphere) and the xz-plane (left), highlighting the presence of small-scale magnetic structures at $z \lesssim 0.01R_\odot$, consistent with Hudson et al. [20]. We have 100 different realizations of the total magnetic field by reshuffling the random parameters in [25] every 100 particles. We set $L_{\min} = 10^{-3}R_\odot$ and $L_{\max} = L = 0.06R_\odot$, with L being the box size of the domain L^3, while the largest horizontal scale of the magnetic photospheric structures is set to $L_s = 0.003\ R_\odot \simeq 2$ Mm. We considered different values of $\sigma^2 = \sigma'^2/B_0^2 = 0.1, 1, 10$, with $\sigma'^2 = \langle \delta\mathbf{B}^2(x,y,z)\rangle$, where $\langle\cdot\rangle$ indicates the average over the different magnetic field realizations.

Figure 1: *Left panel:* Decomposition of the particle velocity vector defined by the angles ϕ and θ together with the magnetic field magnitude in the 3D domain (with logarithmic color scale in Gauss). *Top right panel:* Average angle $\langle\theta\rangle_\perp$ (in degrees) as a function of the altitude z. *Bottom right panels:* Magnetic field magnitude (colorbar) and lines (in black) at the $y = 0.003R_\odot$ (left panel) and $z = 0.003R_\odot$ plane (right panel). All the plots are obtained with $\sigma^2 = 10$.

3. Numerical setup

The numerical simulations are carried out using the PLUTO code for astrophysical gas dynamics [21]. Building on our previous work [13], we extend the 2D domain to 3D, using a cubic domain of size L^3 with a grid resolution of 100^3, corresponding to a spatial resolution of $\simeq 418$ km. In particular, the computational box spans the ranges $-0.03 < x/R_\odot < 0.03$, $0 < y/R_\odot < 0.06$, and $0 < z/R_\odot < 0.06$. Periodic boundary conditions are applied in the x- and the y- directions, while outflow boundary conditions are used along the z-direction, allowing particles to escape the domain either by precipitating onto the solar surface or by leaving the low corona without further interaction. $N_{\rm inj} = 10,000$ GCR protons are injected with an isotropic velocity distribution, placing one test particle per cell over an xy-plane at two distinct altitudes: $z = z_{\rm up} = 0.05R_\odot \sim 35000$

km (into the laminar magnetic field region) and $z = z_{down} = 0.005R_\odot \sim 3500$ km (into the magnetically braided region). The particle trajectories are integrated using the Boris algorithm up to $t_{stop} = 25\, R_\odot/c \sim 58\, s$, which ensures sufficient time for the particles to either interact or escape the domain. The method used to identify and count the number of interacting protons (N_{int}), as well as to determine the density profile, follows the approach described in our previous work [13]. The calculation of the resulting gamma-ray flux is slightly modified to account for open magnetic field lines now included in the model. Nonetheless, it still starts from the expression of [26]:

$$\Phi_\gamma(E_\gamma) \equiv \frac{dN_\gamma}{dE_\gamma} = \frac{2\pi R_\odot^2}{L^2}\left(\frac{R_\odot}{R_{1AU}}\right)^2 cn_p \int_{E_\gamma}^\infty \sigma_{pp}(E_p) J_p(E_p) F_\gamma\left(\frac{E_\gamma}{E_p}, E_p\right)\frac{dE_p}{E_p}, \qquad (2)$$

where $J_p(E_p) = N_{int}(E_p)/N_{inj} \times (E_p^2 dN/dE_p)_{obs} \times 1/(E_p^2 c)$ incorporates the simulation results via the ratio $N_{int}(E_p)/N_{inj}$, averaged over the two injection altitudes z_{up} and z_{down} [for further details on the method see 13].

4. Results

The number of interacting N_{int} (escaping N_{esc}) both divided to N_{inj} as a function of σ^2 are shown by the solid (dashed) lines is shown by the left panel of Fig. 2. The results for the 100 GeV (10 TeV) GCR case injected at $z = z_{up}$ and $z = z_{down}$ are plotted with red (blue) and magenta (black) lines, respectively. The panel shows that N_{int} increases with σ^2 when protons are injected at $z = z_{down}$, as the small-scale magnetic structures in the photosphere enhance the GCRs residence time. Correspondingly, N_{esc} decreases (see the dashed lines of the same colors). N_{int} is smaller and remains approximately constant with σ^2 when protons are injected at $z = z_{up}$, as most GCRs escape upwards the computational domain ($N_{esc}/N_{inj} \sim 1$) along the laminar magnetic field due to the large r_g (see right panel of Fig. 2) before interacting.

Figure 3 shows the distribution of the θ and ϕ angles (as defined in the left panel of Fig. 1) of the velocity vectors of protons at t_{int}, for simulations with $\sigma^2 = 10$ and for 100 GeV (left panel) and 10 TeV (right panel) protons injected at $z = z_{down}$. Due to momentum conservation, the gamma-ray emission direction closely follows the proton interaction direction. The panels reveal an energy-dependent emission pattern on the solar disk, already observed by Fermi-LAT [6]. In both energy cases, gamma-rays are emitted across the full ϕ range. However, for the 10 TeV case (right panel), the emission in θ is more narrowly confined ($70° < \theta < 90°$), indicating that most protons interact in directions nearly tangent to the bottom of the photosphere (corresponding to the xy-plane in the left panel of Fig. 1), while at 100 GeV (left panel), the emission covers a broader range, down to $\theta \approx 50°$.

Figure 4 presents the solar disk gamma-ray flux derived from our simulations with $B_0 = 5$ G and different σ^2: 0.1 (green), 1 (brown), and 10 (orange diamonds, leading to a maximum photospheric magnetic field $B_{max} \sim 100$ G). Results with $\sigma^2 = 10$ and $B_0 = 50$ G (leading to a $B_{max} \sim 1$ kG) are shown by orange stars. The flux is compared to Fermi-LAT observations with and without solar flares [purple and black points, 6], HAWC observations [blue, 4], and the maximum efficiency estimate at 1 AU (solid black line). The latter is calculated as $\phi_\gamma(1AU) \approx (E_p^2 dN/dE_p)_{obs}(R_\odot/R_{1AU})^2(E_\gamma/E_p)$, where the proton energy E_p is ten times the emitted gamma-ray energy E_γ (i.e., $E_\gamma/E_p \sim 1/10$). Results below $E_\gamma < 10$ GeV are omitted due to limited spatial resolution. The gamma-ray flux
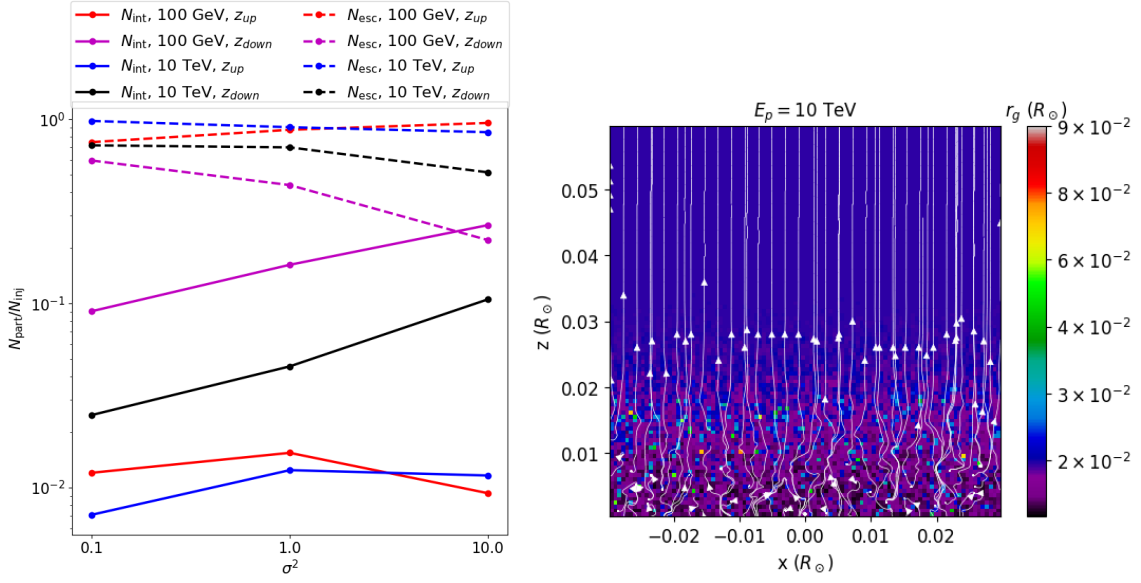
Figure 2: *Left panel:* Number of interacting ($N_{\text{int}}/N_{\text{inj}}$, solid lines) and escaping ($N_{\text{esc}}/N_{\text{inj}}$, dashed lines) GCR protons as a function of σ^2 for particles injected at $z = z_{\text{up}}$ (red and magenta lines) and $z = z_{\text{down}}$ (blue and black lines), with energies of 100 GeV (red and blue) and 10 TeV (magenta and black). *Right panel:* Gyroradius r_g of 10 TeV GCRs over the simulation domain (colorbar) with magnetic field lines (in white).
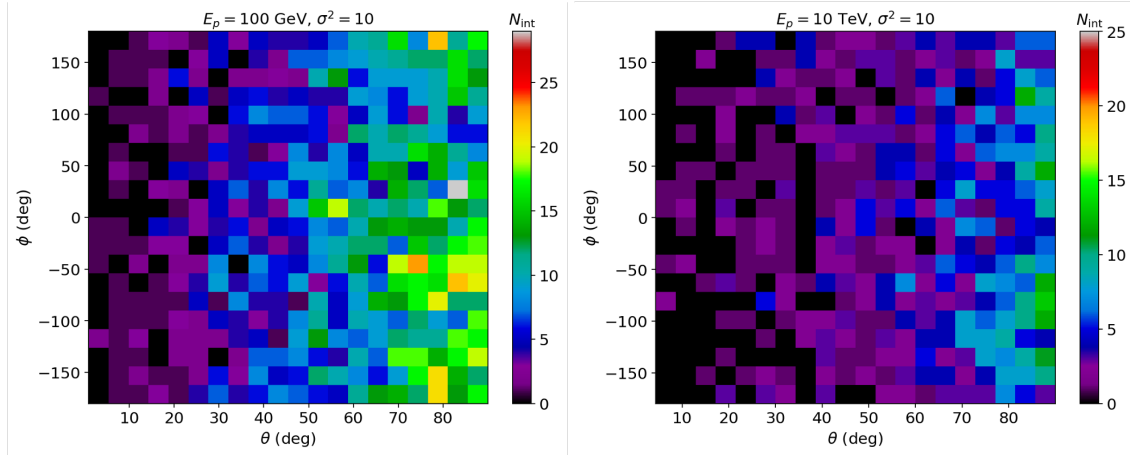

Figure 3: *Left panel*: Distribution of the θ and ϕ angles of the velocity vector at t_{int} of GCRs with energy 100 GeV injected at $z = z_{\text{down}}$ with $\sigma^2 = 10$. *Right panel:* Same as left panel but for 10 TeV GCR protons.

increases with σ^2 (as N_{int} increases, also found in [13]) across the entire energy range up to the TeV energies observed by HAWC, and for higher σ^2 a flattening appears in the dip region ($\sim 30 - 100$ GeV), as highlighted in the inset.

5. Conclusions and outlooks

This works extends [13] by introducing a synthetic magnetic field model characterized by open magnetic field lines at the top which become increasingly horizontal near the sun surface, allowing
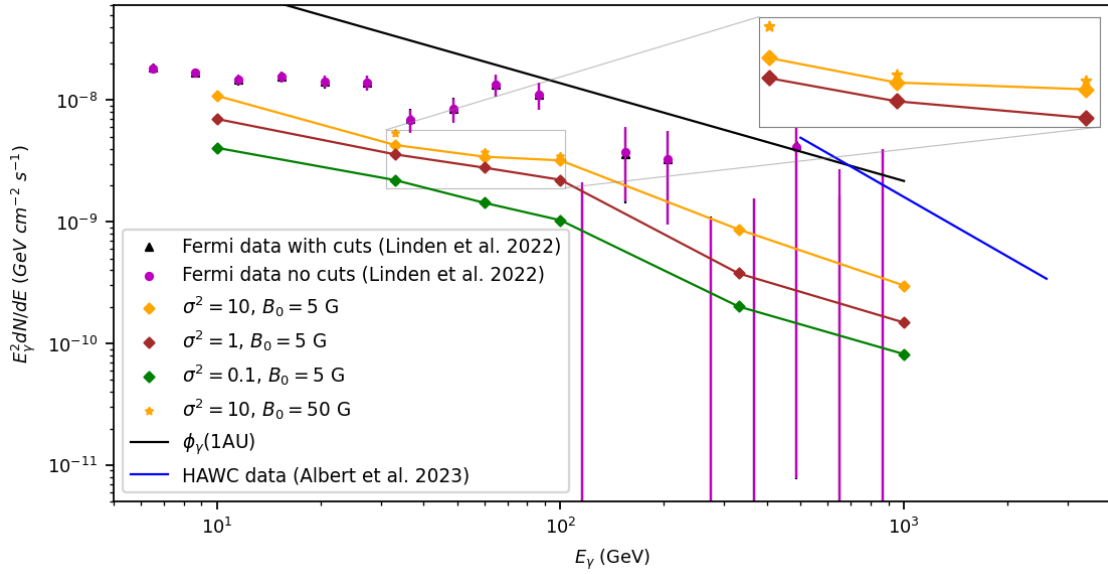
Figure 4: Solar disk gamma-ray flux from simulations with $B_0 = 5$ G and $\sigma^2 = 0.1$ (green), 1 (brown), and 10 (orange diamonds), and for $\sigma^2 = 10$ with $B_0 = 50$ G (orange stars). Also shown are Fermi-LAT observations with and without solar flares [purple and black points; 6], HAWC observations [blue points; 4], and the estimated maximum efficiency flux at 1 AU (solid black line). The inset at the top right zooms in on the dip region ($\sim 30 - 100$ GeV).

GCRs to penetrate the dense photosphere along irregular field lines.

Our simulations confirm that gamma-ray production increases with the magnetic field irregularity (represented by σ^2), but depends on the injection height: protons injected lower, in the non-vertical region, are more likely to interact, whereas higher injection leads to escape along open field lines. We show that small-scale magnetic structures in the photosphere play a crucial role in reproducing the overall order or magnitude and trend of the solar disk gamma-ray flux observed by Fermi-LAT and HAWC, especially in reproducing the observed spectral dip/rebrightening around 30-100 GeV. As σ^2 increases, the gamma-ray flux in this region flattens, a feature absent in previous models. The energy-dependent solar disk gamma-rays emission pattern showing a broader emission pattern at lower energies and a more confined, tangent-plane-aligned emission at higher energies, is roughly consistent with Fermi-LAT observations [6] and numerical simulations [13].

While the present model does not evolve the magnetic field dynamically and lacks fully closed loops that could further trap GCRs, it reflects the irregularity seen in observations [17, 18] and MHD simulations [20]. This highlights the dominant role of photospheric magnetic structures in gamma-ray production. Future work will focus on coupling with dynamic MHD models to include interchange reconnection, offering a more complete picture of solar disk gamma-ray emission.

Acknowledgements

References

[1] Seckel, D., Stanev, T., & Gaisser, T. K. 1991, ApJ, Signatures of Cosmic-Ray Interactions on the Solar Surface, 382, 652. doi:10.1086/170753

[2] Abdo, A. A., Ackermann, M., Ajello, M., et al. 2011, ApJ, Fermi Large Area Telescope Observations of Markarian 421: The Missing Piece of its Spectral Energy Distribution, 736, 2, 131. doi:10.1088/0004-637X/736/2/131

[3] Linden, T., Zhou, B., Beacom, J. F., et al. 2018, Phys. Rev. Lett., Evidence for a New Component of High-Energy Solar Gamma-Ray Production, 121, 13, 131103. doi:10.1103/PhysRevLett.121.131103

[4] Albert, A., Alfaro, R., Alvarez, C., et al. 2023, Phys. Rev. Lett., Discovery of Gamma Rays from the Quiescent Sun with HAWC, 131, 5, 051201. doi:10.1103/PhysRevLett.131.051201

[5] Ng, K. C. Y., Beacom, J. F., Peter, A. H. G., et al. 2016, Phys. Rev. D, First observation of time variation in the solar-disk gamma-ray flux with Fermi, 94, 2, 023004. doi:10.1103/PhysRevD.94.023004

[6] Linden, T., Beacom, J. F., Peter, A. H. G., et al. 2022, Phys. Rev. D, First observations of solar disk gamma rays over a full solar cycle, 105, 6, 063013. doi:10.1103/PhysRevD.105.063013

[7] Acharyya, A., Adelfio, A., Ajello, M., et al. 2025, Surprising Variation of Gamma Rays from the Sun over the Solar Cycle Revealed with Fermi-LAT, arXiv:2505.06348. doi:10.48550/arXiv.2505.06348

[8] Arsioli, B. & Orlando, E. 2024, ApJ, Yet Another Sunshine Mystery: Unexpected Asymmetry in GeV Emission from the Solar Disk, 962, 1, 52. doi:10.3847/1538-4357/ad1bd2

[9] Tang, Q.-W., Ng, K. C. Y., Linden, T., et al. 2018, Phys. Rev. D, Unexpected dip in the solar gamma-ray spectrum, 98, 6, 063019. doi:10.1103/PhysRevD.98.063019

[10] Cannady, N. W. 2022, 37th International Cosmic Ray Conference, Low-energy gamma-ray observations above 1 GeV with CALET on the International Space Station, 604. doi:10.22323/1.395.0604

[11] Zhou, B., Ng, K. C. Y., Beacom, J. F., et al. 2017, Phys. Rev. D, TeV solar gamma rays from cosmic-ray interactions, 96, 2, 023015. doi:10.1103/PhysRevD.96.023015

[12] Li, J.-T., Beacom, J. F., Griffith, S., et al. 2024, ApJ, Small-scale Magnetic Fields Are Critical to Shaping Solar Gamma-Ray Emission, 961, 2, 167. doi:10.3847/1538-4357/ad158f

[13] Puzzoni, E., Fraschetti, F., Kóta, J., et al. 2024, ApJ, Role of Magnetic Arcades in Explaining the Puzzle of the Gamma-Ray Emission from the Solar Disk, 973, 2, 118. doi:10.3847/1538-4357/ad65ea

[14] Ng, K. C. Y., Hillier, A., & Ando, S. 2024, TeV Solar Gamma Rays as a probe for the Solar Internetwork Magnetic Fields, arXiv:2405.17549. doi:10.48550/arXiv.2405.17549

[15] Alfaro, R., Alvarez, C., Arteaga-Velázquez, J. C., et al. 2024, ApJ, Exploring the Coronal Magnetic Field with Galactic Cosmic Rays: The Sun Shadow Observed by HAWC, 966, 1, 67. doi:10.3847/1538-4357/ad3208

[16] Morton, R. J., Sharma, R., Tajfirouze, E., et al. 2023, Reviews of Modern Plasma Physics, Alfvénic waves in the inhomogeneous solar atmosphere, 7, 1, 17. doi:10.1007/s41614-023-00118-3

[17] Danilovic, S., Schüssler, M., & Solanki, S. K. 2010, A&A, Probing quiet Sun magnetism using MURaM simulations and Hinode/SP results: support for a local dynamo, 513, A1. doi:10.1051/0004-6361/200913379

[18] Stenflo, J. O. 2013, A&A, Horizontal or vertical magnetic fields on the quiet Sun. Angular distributions and their height variations, 555, A132. doi:10.1051/0004-6361/201321608

[19] Rempel, M. 2014, ApJ, Numerical Simulations of Quiet Sun Magnetism: On the Contribution from a Small-scale Dynamo, 789, 2, 132. doi:10.1088/0004-637X/789/2/132

[20] Hudson, H. S., MacKinnon, A., Szydlarski, M., et al. 2020, MNRAS, Cosmic ray interactions in the solar atmosphere, 491, 4, 4852. doi:10.1093/mnras/stz3373

[21] Mignone, A., Bodo, G., Massaglia, S., et al. 2007, ApJS, PLUTO: A Numerical Code for Computational Astrophysics, 170, 1, 228. doi:10.1086/513316

[22] Schad, T. A., Petrie, G., Kuhn, J., et al. 2024, Science Advances, Mapping the Sun's coronal magnetic field using the Zeeman effect, 10, 37, eadq1604. doi:10.1126/sciadv.adq1604

[23] González-Avilés, J. J., Guzmán, F. S., Fedun, V., et al. 2018, ApJ, I. Jet Formation and Evolution Due to 3D Magnetic Reconnection, 856, 2, 176. doi:10.3847/1538-4357/aab36f

[24] Giacalone, J. 2021, ApJ, The Transport Equation for the Dispersal of Passive Tracers in a Nonuniform Turbulent Fluid: Numerical Simulations, 912, 2, 83. doi:10.3847/1538-4357/abf0b2

[25] Giacalone, J. & Jokipii, J. R. 1999, ApJ, The Transport of Cosmic Rays across a Turbulent Magnetic Field, 520, 1, 204. doi:10.1086/307452

[26] Kelner, S. R., Aharonian, F. A., & Bugayov, V. V. 2006, Phys. Rev. D, 74, 3, 034018. doi:10.1103/PhysRevD.74.034018